Using a Quasipotential Transformation for Modeling Diffusion Media in Polymer-Electrolyte Fuel Cells

Adam Z. Weber[1,*,z] and John Newman[1,2,**]

[1]Lawrence Berkeley National Laboratory, Berkeley, California 94720
[2]Department of Chemical Engineering,
University of California, Berkeley, California 94720-1462, USA

In this paper, a quasipotential approach along with conformal mapping is used to model the diffusion media of a polymer-electrolyte fuel cell. This method provides a series solution that is grid independent and only requires integration along a single boundary to solve the problem. The approach accounts for nonisothermal phenomena, two-phase flow, correct placement of the electronic potential boundary condition, and multilayer media. The method is applied to a cathode diffusion medium to explore the interplay between water and thermal management and performance, the impact of the rib-to-channel ratio, and the existence of diffusion under the rib and flooding phenomena.

Keywords: Modeling, PEFC, gas-diffusion layer, cathode, water management

[z] Corresponding author: e-mail: azweber@lbl.gov

1. Introduction

Mathematical modeling is ideally suited for understanding and quantifying the complex interplay between water and thermal in polymer-electrolyte fuel cells (PEFCs). Typical PEFCs operate below 100°C, meaning that water exists both as a liquid and a vapor. Furthermore, a PEFC produces liquid water at the cathode as a product of the electrochemical reduction of oxygen using protons generated by hydrogen oxidation

$$4H^+ + 4e^- + O_2 \rightarrow 2H_2O \tag{1}$$

This product water is formed on the cathode of the PEFC, and it must be removed before it accumulates and blocks passage of reactant oxygen to the cathode catalyst layer. On the other hand, the proton-conducting membrane used in PEFCs requires hydration in order to conduct efficiently. Intimately involved with the above competing water-management issues is thermal management, where temperature gradients can drive water movement through a heat-pipe effect [38]. Many models have been generated to examine the above interplays and are summarized in recent reviews by Newman and coworkers [36, 41] and those in this issue.

The complex needs of water management results in complex materials used as backing layers for the support of the catalyst layers and as shown in Figure 1. These so-called diffusion media (DM) are typically composed of a macroporous gas-diffusion layer (GDL) and a microporous layer (MPL). In addition, each layer contains mixed wettability composed of hydrophilic (carbon) and hydrophobic (Teflon) moieties. Various models have been developed to account for the two-phase flow in these materials, where there is a lack of experimental data [36, 9, 18, 19, 26, 33, 7, 42, 10, 31, 21, 37]. While these models are aimed at determining the dependent transport properties and medium saturation or liquid-volume fraction, they must be utilized in a macroscopic framework. Such a framework often employs discretization techniques (*e.g.*, finite-

differencing and computational fluid dynamics). Furthermore, the problem is multidimensional due to the geometry of the gas flowfields in contact with the backing layer. This rib/channel structure creates a problem as highlighted in Figure 1.

As seen, the domain to be studied in this article is the cathode DM. The cathode is chosen because it is perhaps the most limiting layer in a PEFC due to the sluggish oxygen-reduction-reaction kinetics, the need to remove the generated liquid water and that coming from the anode due to an electroosmotic flux, and the fact that PEFCs use air in which oxygen is already diluted. Although the full problem is three-dimensional, a two-dimensional approach can be used due to the much longer length-scale of the channel compared to the other dimensions. If one then uses enough segments in the channel or *z*-direction, then the composition in the gas channel can be taken as constant in each segment. The problem outlined in Figure 1 has been investigated previously for the cathode DM [20, 43, 6, 17, 22, 35, 15]. However, in those analyses, differencing techniques and full numerical solutions were employed. In this article, we utilize a quasipotential transformation and conformal mapping to reduce the problem to a set of analytic series solutions, where the coefficients only require integration along a single boundary. Such an approach has several benefits including removal of the singularity of adjacent conducting and insulating planes, a computationally fast and efficient solution procedure, a grid-independent accurate solution, and a more robust solution procedure involving ordinary-differential equations (ODEs) instead of partial-differential equations (PDEs).

Quasipotential transformations have been discussed previously in terms of modeling electrochemical phenomena as well as the Stefan-Maxwell equations [20, 34, 3, 4, 29]. Such an approach has been applied to the geometry in Figure 1 [20], yet without considering two-phase flow effects, multi-layer DM, nonisothermal phenomena, and the fact that the electronic current

flows through the rib and not the channel (where all of the other species occur). All of these limitations are removed in the following analysis. However, there are still fundamental limitations when using a quasipotential transformation including the need for steady-state or quasi-steady-state behavior, equilibrated homogeneous reactions, constant variable values at one boundary, the overall fluxes to be related to one another, and no open-flow convection. Luckily, the case of the DM fits within these limitations as discussed in more detail in the following sections.

The outline of the paper is as follows. First, the problem statement is outlined with the governing equations and boundary conditions. Next, the definition of the quasipotential is made, and the reduction of the governing equations to Laplace's equation and a set of first-order nonlinear ordinary-differential equations is shown. Next, the geometric problem is solved using conformal mapping and analytic functions where possible. After discussing treatment of the electronic potential using a second quasipotential transformation and conformal mapping, the overall solution procedure is outlined. This is followed by a discussion on the treatment of multilayer DM. Next, various simulation results are analyzed to see the impact of the ribs on performance and understand the interplay between water and thermal management and performance. Finally, some remarks about future work and limitations of the presented approach are discussed.

2. Problem Statement

The problem statement in terms of geometry and boundary conditions is summarized in Figure 2. In total, there are seven principle variables: the mole fractions of oxygen, nitrogen, and water vapor, y_{O_2}, y_{N_2}, and y_{H_2O}, respectively; the temperature, T; the electronic potential, Φ;

and the liquid and gas pressures, p_L and p_G, respectively. If the various fluxes ($\mathbf{N}_i$ for the gas and liquid species, **i** for current density, and **q** for thermal energy) are taken to be variables as well, this results in a set of first-order equations for both the fluxes and the above variables. The flux conservation equations for the DM are

$$\nabla \cdot \mathrm{N}_i = 0 \tag{2}$$

for oxygen and nitrogen,

$$\nabla \cdot \mathrm{N}_\mathrm{w} = \nabla \cdot \mathrm{N}_\mathrm{L} + \nabla \cdot \mathrm{N}_{\mathrm{H_2O}} = 0 \tag{3}$$

for water, where it has been assumed that rate of condensation/evaporation is large enough (due to the fast interchange and substantial interfacial surface area between liquid and vapor) that local equilibrium can be assumed, and

$$\nabla \cdot \mathbf{i} = 0 \tag{4}$$

for current density and

$$\nabla \cdot \mathbf{q} = 0 \tag{5}$$

for thermal energy. It should be noted that ohmic heating, which is expected to be small in the DM [38], is neglected in the thermal-energy balance due to its incompatibility with a quasipotential transformation (it is a second-order effect). Furthermore, since local equilibrium is assumed between liquid and vapor, an equilibrium equation has to be added to the set of governing equations

$$\overline{V}_\mathrm{L}\left(p_\mathrm{L} - p_\mathrm{G}\right) = RT \ln\left(\frac{p_\mathrm{G} y_{\mathrm{H_2O}}}{p^\mathrm{o}_\mathrm{vap}}\right) \tag{6}$$

where $\overline{V}_{\mathrm{L}}$ is the partial molar volume of water, R is the ideal-gas constant, and $p^{\mathrm{o}}_{\mathrm{vap}}$ is the vapor pressure of water over a planar interface. The above equation considers the effect of menisci on the water vapor pressure. Equation 6 can be seen as a combination of the Kelvin and Young-Laplace equations [8]. The former accounts for pore radii and contact angle and the latter allows for the substitution of the capillary pressure for such effects. Thus, the impact of pore size and contact angle are implicitly accounted for.

The above fluxes are related to the set of transport equations. For the gas species, generalized Stefan-Maxwell equations are used with Knudsen and pressure diffusion considered [5, 40],

$$\nabla y_i = -\frac{y_i}{RT}\left(\frac{RT}{p_{\mathrm{G}}} - \frac{M_i}{\rho}\right)\nabla p_{\mathrm{G}} + \sum_{j\neq i}\frac{1}{c_T \varepsilon D^{\mathrm{eff}}_{i,j}}\left(y_i \mathbf{N}_j - y_j \mathbf{N}_i\right) - \frac{1}{c_T \varepsilon D^{\mathrm{eff}}_{\mathrm{i,j}}}\mathbf{N}_i \tag{7}$$

where ρ is the density of the gas phase, M_i is the molar mass of species i, c_T is the total gas-phase concentration, ε is the gas-phase volume fraction, $D^{\mathrm{eff}}_{i,j}$ is the effective binary diffusion coefficient between species i and j, and $D^{\mathrm{eff}}_{K_i}$ is the effective Knudsen diffusion coefficient of species i. The effective diffusion coefficients are corrected for typically corrected for tortuosity using Bruggemann expression:

$$D^{\mathrm{eff}}_{i,j} = \frac{1}{\tau} D_{i,j} = \varepsilon^{0.5} D_{i,j} \tag{8}$$

The above form of the Stefan-Maxwell equations allow for a smooth, continuous transition between the modeling of both slip and ordinary diffusion through the range of pore sizes of the DM.

One of the three gas-species Stefan-Maxwell equations can be replaced by the sum of the mole fractions,

$$\sum y_i = 1 \tag{9}$$

For the liquid phase, a flux form of Darcy's law is used

$$\mathbf{N}_{\mathrm{L}} = -\frac{k_{\mathrm{L}}}{\bar{V}_{\mathrm{L}}\mu_{\mathrm{L}}}\nabla p_{\mathrm{L}} \tag{10}$$

where μ_{L} and k_{L} are the partial molar volume, viscosity, and effective permeability of liquid water in the DM. Similarly, Darcy's law is used for the gas phase to determine the gas pressure

$$\sum M_i \mathbf{N}_i = -\frac{\rho k_{\mathrm{G}}}{\mu_{\mathrm{G}}}\nabla p_{\mathrm{G}} \tag{11}$$

For the current density, Ohm's law is used

$$\mathbf{i} = -\sigma\nabla\Phi \tag{12}$$

where σ is the effective electronic conductivity. Finally, for thermal energy, the flux is given by

$$\mathbf{q} = -k_T\nabla T + H_{\mathrm{G}}\mathbf{N}_{\mathrm{G}} + H_{\mathrm{L}}\mathbf{N}_{\mathrm{L}} \tag{13}$$

where k_T is the effective thermal conductivity and H_k is the enthalpy of phase *k*.

The above expressions contain dependent variables that will change throughout the DM. While many of these are known functions of the other variables (*e.g.*, viscosity dependence on temperature or concentration dependence of the gas-phase binary diffusion coefficients) [1, 28], some of them require the use of a submodel for their evaluation. Prime among this second set of dependent variables are the effective permeabilities and the gas-phase volume fraction. To determine these values, a two-phase flow model previously detailed by us is utilized [37].

Essentially, this model uses a cut-and-random-rejoin bundle-of-capillaries approach where the pressure difference between the liquid and gas phases is used along with the DM pore-size distribution and a binary hydrophilicity (wettability) distribution to determine their values. For the scope of this paper, it is sufficient to know that the various dependent variables are calculated from the independent variables and structural properties where necessary, thereby making the problem highly nonlinear.

In terms of boundary conditions, most of the boundaries are insulating as shown in Figure 2. For the gas channel, the six primary variable values are set, including the gas and liquid pressures (set to be equal), the gas mole fractions, and the temperature. The sole exception is that of the electronic potential, which has the opposite rib/channel boundary conditions than the other components. Since this variable does not impact the other ones except at the boundaries, it can be treated using a separate, parallel analysis as discussed below. The same cannot be said for the temperature boundary condition, which is expected to have influence at both the rib and the channel, the former due to conduction and the latter to convection. As noted, these effects are essentially both applied at the gas channel and this represents a limitation of the quasipotential approach. The justification for constant values is due to the implicit assumption of using a pseudo 3-D or 1+2-D dimensional approach where the channel is divided into segments that contact each other only at the boundaries through material and energy balances.

For the cathode catalyst-layer boundary, the five fluxes (equations 2 thru 5) are set. The catalyst layer is treated as an interface (*i.e.*, a uniform reaction-distribution is assumed). The oxygen-reduction-reaction rate is given by Tafel kinetics [23], which, when written in terms of the oxygen flux using Faraday's law, results in a boundary condition for the flux of oxygen

$$\mathbf{N}_{\mathrm{O}_2} = -4Fat_{\mathrm{CL}} i_0 \left(p_{\mathrm{O}_2}\right)^{0.8} \exp\left(-\frac{F}{RT}\left(\Phi - \Phi_2 - U^{\theta}\right)\right)\left(1 - S_{\mathrm{CL}}\right) \tag{14}$$

where at_{CL} is the specific surface area for reaction, i_0 is the exchange current density, p_{O_2} is the partial pressure of oxygen, F is faraday's constant, Φ_2 is the electrolyte potential, U^{θ} is the standard potential for the reaction, and S_{CL} is the saturation (amount of pore space filled by liquid) of the catalyst layer and depends on the difference between the liquid and gas pressures using the two-phase model in the catalyst layer. For a physical representation, a value of $S_{CL} = 1$ means that there is no oxygen access to the catalyst sites and thus the current density is zero (the limiting current is reached). Similarly, proton mobility is a function of water content and if the membrane is dry, then a proton limiting current can be reached. This effect is accounted for in equation 13 by the value of Φ_2. The value of Φ_2 is set in this paper, where, to be rigorous, it should be allowed to vary and calculated using detailed membrane and catalyst-layer models as well as consideration of the anode side of the PEFC; however, such a treatment is beyond the scope of this paper.

For the current-density boundary condition, Faraday's law results in

$$\mathbf{i} = -4F\mathbf{N}_{O_2} \tag{15}$$

Faraday's law can also be used for the water flux, resulting in a boundary condition of

$$\mathbf{N}_w = -\mathbf{N}_{O_2}\left(2 + 4\beta_w\right) \tag{16}$$

where β_w signifies the net flux of water per proton flux through the membrane from anode to cathode. Since nitrogen does not participate in the reaction, its flux is set equal to zero

$$\mathbf{N}_{N_2} = 0 \tag{17}$$

Finally, the temperature boundary condition can be given by

$$\mathbf{q} = -4F\mathbf{N}_{\mathrm{O}_2}\left(\left(\Phi - \Phi_2 - U^{\theta}\right) + \Pi\right) - 4F\mathbf{N}_{\mathrm{O}_2}\beta_{\mathrm{q}}\left(U_H - \Phi_0\right) - H_{\mathrm{w}}\mathbf{N}_{\mathrm{O}_2}\left(2 + 4\beta_{\mathrm{w}}\right) \tag{18}$$

where Π and U_H are the Peltier coefficient and enthalpy potential for the oxygen reduction reaction, respectively, Φ_0 is the set potential at the rib, and β_{q} is the dimensionless heat transferred through the membrane. The first term is due to heat generation, the second term is due to the thermal energy transferred from the membrane and the anode side, and the third term is the enthalpy carried into the DM from the water phase.

Equations 2 thru 18 define the problem in terms of governing equations and boundary conditions. Besides the various DM properties like porosity and pore-size distribution, one must set the liquid and gas pressures, the temperature, and the nitrogen mole fraction at the gas channel, the electronic potential at the rib, and the values of Φ_2, β_{q}, and β_{w} at the catalyst layer. In reality, these last three values will change depending on location (*x*-direction), however, they will be taken to be uniform for the subsequent analysis.

3. Chemical model and quasipotential definition

The approach to solving the problem is to use a set of two quasipotential transformations, Q_Φ for the electronic potential and Q for the rest of the variables. Essentially, these transformations separate the problem into two distinct categories: chemical problems and geometric problems. In the rest of this section and the next, the analysis for the variables besides the electronic potential is given; the electronic potential is treated in a later section.

First, the quasipotential, Q, is defined in terms of the oxygen flux since oxygen is the most important parameter in the cathode DM

$$\mathbf{N}_{\mathrm{O}_2} = \nabla Q \tag{19}$$

Because the fluxes in the DM are constant (see the conservation equations 2 thru 5), and at the boundaries each flux is related to the oxygen flux (see equations 15 thru 18), substitution of equation 19 into the conservation equations utilizing the boundary flux values results in Laplace's equation

$$\nabla^2 Q = 0 \tag{20}$$

This sets up the geometric problem, which is discussed and solved in the next section.

For the chemical problem, in light of the simplification to Laplace's equation and the constant fluxes, the flux of each component throughout the domain will remain uniform and given by the boundary expressions (equations 15 thru 18) [29, 4]. To develop the chemical-model equations, one can start by substituting the boundary expressions into their respective transport equations (equations 7, 10, 11, and 13). Then, using the chain rule,

$$\nabla Y = \left(\frac{\partial Y}{\partial x}, \frac{\partial Y}{\partial y} \right) = \frac{dY}{dQ} \left(\frac{\partial Q}{\partial x}, \frac{\partial Q}{\partial y} \right) = Y' \nabla Q \tag{21}$$

the gradient is rewritten in terms of the quasipotential, and the spatial derivative of the quasipotential will cancel, resulting in a set of nonlinear first order ODEs which depend only on Q.

Enacting the above procedure results in the following set of equations: the equation for nitrogen (equations 7 and 17) becomes

$$-y'_{\mathrm{N}_2} - \left(\frac{y_{\mathrm{N}_2}}{RT} \left(\frac{RT}{p_{\mathrm{G}}} - \frac{M_{\mathrm{N}_2}}{\rho} \right) + \frac{y_{\mathrm{N}_2} \alpha}{c_T \varepsilon D^{\mathrm{eff}}_{\mathrm{N}_2,\mathrm{H}_2\mathrm{O}} \xi} \right) p'_{\mathrm{G}} - \frac{y_{\mathrm{N}_2}}{c_T \varepsilon D^{\mathrm{eff}}_{\mathrm{N}_2,\mathrm{H}_2\mathrm{O}} \xi} y'_{\mathrm{H}_2\mathrm{O}} = -\frac{y_{\mathrm{N}_2}}{c_T \varepsilon D^{\mathrm{eff}}_{\mathrm{N}_2,\mathrm{O}_2}} - \frac{y_{\mathrm{N}_2} \psi}{c_T \varepsilon D^{\mathrm{eff}}_{\mathrm{N}_2,\mathrm{H}_2\mathrm{O}} \xi} \tag{22}$$

where

$$\alpha = \frac{y_{H_2O}}{RT}\left(\frac{RT}{p_G} - \frac{M_{H_2O}}{\rho}\right)$$

$$\psi = \frac{y_{H_2O}}{c_T \varepsilon D^{eff}_{O_2,H_2O}} \tag{23}$$

$$\xi = \frac{y_{O_2}}{c_T \varepsilon D^{eff}_{O_2,H_2O}} + \frac{y_{N_2}}{c_T \varepsilon D^{eff}_{N_2,H_2O}} + \frac{1}{c_T \varepsilon D^{eff}_{K_{H_2O}}}$$

the equation for liquid pressure (equations 10 and 16) becomes

$$-\frac{k_L}{\overline{V}_{H_2O}\mu_L} p'_L - \frac{1}{\xi} y'_{H_2O} - \frac{\alpha}{\xi} p'_G = -\left(2 + 4\beta_{H_2O}\right) - \frac{\psi}{\xi} \tag{24}$$

the equation for gas pressure (equation 11) becomes

$$\left(\frac{\rho_G k_G}{\mu_G} - \frac{\alpha}{\xi} M_{H_2O}\right) p'_G - \frac{M_{H_2O}}{\xi} y'_{H_2O} = -M_{O_2} - \frac{\psi}{\xi} M_{H_2O} \tag{25}$$

and the equation for temperature (equations 13 and 18) becomes

$$\begin{aligned} -k_T T' - \frac{H_G}{\xi} y'_{H_2O} - \frac{H_G \alpha}{\xi} p'_G - \frac{H_L k_L}{\overline{V}_{H_2O}\mu_L} p'_L = \\ 4F\left(\left(\Phi - \Phi_2 - U\right) + \Pi + \beta_q\left(U_H - \Phi_0\right)\right) - H_G\left(1 + \frac{\psi}{\xi}\right) - H_w \mathbf{N}_{O_2}\left(2 + 4\beta_w\right) \end{aligned} \tag{26}$$

For the oxygen and water-vapor mole fractions equations 9 and 6 are differentiated resulting in

$$y'_{N_2} + y'_{O_2} + y'_{H_2O} = 0 \tag{27}$$

and

$$\overline{V}_L p'_L - \left(\overline{V}_L + \frac{RT}{p_G}\right) p'_G - \left(\overline{V}_L + \frac{RT}{y_{H_2O}}\right) y'_{H_2O} + R\left(-\ln\left(p_G y_{H_2O}\right) + \frac{dp^o_{vap}}{dT}\right) T' = 0 \tag{28}$$

respectively.

Equations 22 thru 28 represent the chemical problem. It should be noted that the quasipotential transformation can only be applied to first order effects in order for the spatial dependence to cancel from the chemical-model equations. This is why ohmic heating has to be ignored, which is a justified assumption given the high conductivity of the DM. Similarly, if one uses the Navier-Stokes equations instead of Darcy's law for convective flow, the quasipotential transformation cannot be applied. Luckily, the DM is a porous medium which can be described by Darcy's law.

In terms of the boundary conditions, at the gas channel where the variables values are set, Q is set equal to zero. To solve the chemical problem, one solves the above initial-value ODE problem numerically to the specified Q value. A sample figure of the variables as a function of Q for the specified initial values and DM properties (see Table I) is shown in Figure 3. From the figure, one can see that most of the deviations are relatively linear until larger values of Q are realized. Furthermore, while one could think of Q as being intimately related to the oxygen partial pressure due to its definition (equation 19), one can see that is not the case at large values due to the interplay among all of the equations.

From Figure 3, it is clear that for the given inlet conditions and material properties, there is a limiting current where the oxygen concentration goes to zero. If one uses Faraday's law and assumes a 250 μm DM, then the limiting current density is equal to about 2.5 A/cm^2. This value is higher than most currently operating PEFCs, thereby suggesting that DM limitations are not the largest. However, this simple analysis does not consider how the values of Φ_2, β_q, and β_w change with current density and other related effects. As shown later though, this simple analysis allows for a quick study of the general effects of medium wettability on performance. Finally, it appears that the flooding and limiting current density is being exacerbated and perhaps

even driven by the decrease in the gas-phase pressure. Although, due to the highly coupled nature of the problem and the variables, such a generalization is not tenable. However, it is a noteworthy observation because many models, especially older ones, assume a uniform gas pressure in the DM, which is obviously a circumspect assumption.

4. Geometric model and quasipotential solution

In the preceding section, the quasipotential transformation is defined and the chemical problem explored. It is shown that for the geometric problem, Laplace's equation is obtained. To solve this problem, the boundary conditions are required. Using the quasipotential transformation, the insulating boundaries remain insulating. As noted, at the gas channel, the value of Q is arbitrarily set to 0. At the catalyst layer, the boundary condition can be written as (see equation 14)

$$\begin{aligned}\nabla Q \cdot n &= -4Fat_{\mathrm{CL}} i_0[Q]\left(p_{\mathrm{G}}[Q] y_{\mathrm{O}_2}[Q]\right)^{0.8} \exp\left(-\frac{F}{RT[Q]}\left(\Phi[Q_\Phi] - \Phi_2 - U^\theta[Q]\right)\right)\left(1 - S_{\mathrm{CL}}[Q]\right) \\ &= -N[Q, Q_\Phi]\end{aligned} \tag{29}$$

where the dependences on the two quasipotentials are shown explicitly and many arise from the effect of temperature on the various properties (*e.g.*, see Table I).

The geometric problem is now completely specified. To solve this problem, conformal mapping is used. The overall procedure is to use Schwartz-Christoffel transformations to transform the initial geometry in the z-plane to the upper half of the w-plane and then into a rectangle in the a-plane [12]. Schematically, this solution procedure is shown in Figure 4, with the boundary conditions noted and the appropriate dimensions marked, where t is the thickness of the DM, L is the length of the DM, and δ represents the dimensionless location of the

rib/channel interface. The origin the *z*-plane is defined at the DM half-thickness for reasons that will become apparent.

The transform from the *w*-plane to the *z*-plane is given by

$$z = C\int_0^w \frac{dw}{\sqrt{w-a}\sqrt{w-b}\sqrt{w-c}\sqrt{w-d}} \tag{30}$$

where the lower case letters correspond to the location of the *z*-plane vertices in the *w*-plane. We have a degree of freedom such that we can arbitrarily assign a value of 1 to *b* (as noted in Figure 4). Due to the origin placement, we also have symmetry between points *a* and *b* and also *c* and *d* [2]. Thus, equation 30 can be written as

$$z = -Ck\int_0^w \frac{dw}{\sqrt{1-w^2}\sqrt{1-k^2w^2}} = -CkF(w;k) \tag{31}$$

where $k = c^{-1}$ and $F(w;k)$ is the incomplete elliptical integral of the first kind [46]. In the above expression, there are two unknowns: *C* and *k*. As noted above, in the *z*-plane, the DM thickness and length are specified. Substituting in the thickness in equation 31 results in

$$C = \frac{-t}{2k\int_0^1 \frac{du}{\sqrt{1-u^2}\sqrt{1-k^2u^2}}} = \frac{-t}{2kK(k)} \tag{32}$$

where $K(k)$ is the complete elliptic integral of the first kind [46]. Next, substituting the length into equation 31 results in a transcendental equation for *k*

$$\frac{2L}{t} = \frac{K(k')}{K(k)} \tag{33}$$

where $k' = \sqrt{1-k^2}$. Thus, *C* and *k* can be solved for and equation 31 can be written as

$$z = \frac{t}{2K(k)} F(w;k) \tag{34}$$

The above transform can be inverted to yield the transform from the *z*-plane to the *w*-plane. Doing this inversion results in [2, 46]

$$w = \mathrm{sn}\left(\frac{2K(k)}{t} z, k \right) \tag{35}$$

where sn is an elliptic function (which is tabulated), and expressions for *u* and *v* can easily be obtained by known elliptic-function identities [46, 2, 30]. Now, all of the points in *w*-plane have been determined. Specifically,

$$a = -b = -1;\ d = -c = -\frac{1}{k};\ e = -\frac{\mathrm{dn}\left(\frac{2K(k)}{t} \delta L, k' \right)}{1 - k'^2 \,\mathrm{sn}^2\left(\frac{2K(k)}{t} \delta L, k' \right)} \tag{36}$$

Next, one must transform the *w*-plane into the *a*-plane. The resulting Schwartz-Christoffel transformation is

$$a = -\int_{-1}^{w} \frac{dw}{\sqrt{w-1}\sqrt{w+1}\sqrt{w-c}\sqrt{w-e}} \tag{37}$$

where this integral has to be evaluated numerically.

Finally, before solving the problem in the *a*-plane, the boundary conditions must be transformed. Since insulators remain insulators and Dirichlet boundary conditions remain intact through the transformations, only the boundary-condition at the catalyst layer (equation 29) has to be transformed. This transformation is done by examining the respective transformations at the catalyst-layer boundary (**BC** in Figure 4),

$$\left.\frac{da}{dw}\right|_{\mathbf{BC}} = \frac{i}{\sqrt{u-1}\sqrt{u+1}\sqrt{u-c}\sqrt{u-e}}$$
$$\left.\frac{dz}{dw}\right|_{\mathbf{BC}} = \frac{t}{2kK(k)}\frac{i}{\sqrt{u-1}\sqrt{u+1}\sqrt{u-c}\sqrt{u+c}} \tag{38}$$

and noting that in the *z*-plane

$$\left.\frac{\partial Q}{\partial x}\right|_{\mathbf{BC}} = \mathrm{Re}\left\{\frac{dQ}{da}\frac{da}{dw}\frac{dw}{dz}\right\} = -N\left[Q,Q_{\Phi}\right] \tag{39}$$

Doing the above analysis results in a catalyst-layer boundary condition in the *a*-plane of

$$\left.\frac{\partial Q}{\partial a_r}\right|_{\mathbf{BC}} = -\frac{t}{2kK(k)}N\left[Q,Q_{\Phi}\right]\frac{\sqrt{u-e}}{\sqrt{u+c}} = G\left[Q,Q_{\Phi},a_i\right] \tag{40}$$

Now that the problem has been transformed into the *a*-plane, one can write the solution using separation of variables

$$Q = c_0 a_r + \sum_{n=1}^{\infty} c_n \cos\left(\frac{\pi n}{a_{\mathbf{C}}}a_i\right)\sinh\left(\frac{\pi n}{a_{\mathbf{C}}}a_r\right) \tag{41}$$

where $a_{\mathbf{C}}$ denotes the point of **C** in the *a*-plane (see Figure 4). The Fourier coefficients are then given by

$$c_0 = \frac{\int_0^{a_{\mathbf{C}}} G\left[Q,Q_{\Phi},a_i\right]da_i}{a_{\mathbf{C}}};\quad c_n = \frac{2\int_0^{a_{\mathbf{C}}} \cos\left(\frac{\pi n}{a_{\mathbf{C}}}a_i\right)G\left[Q,Q_{\Phi},a_i\right]da_i}{\pi n \cosh\left(\frac{\pi n}{a_{\mathbf{C}}}a_{\mathbf{B}}\right)} \tag{42}$$

It is obvious that to solve the problem, all that must be done is to complete the above integrations along **BC** using the values of the quasipotentials and the value of $G\left[Q,Q_{\Phi},a_i\right]$ given by equation 40.

5. Treatment of the electronic potential

As noted above, the electronic potential has its boundary condition at the rib and not the channel, since the channel acts as an electronic insulator (see Figure 2). Because the potential only interacts with the other variables at the catalyst-layer boundary (the electronic conductivity is taken as uniform in the DM), it can be set up as its own independent problem.

In a similar fashion to the quasipotential analysis above, an electronic quasipotential, Q_Φ, can be setup, where again it will be related to the oxygen flux (see equation 19). Substitution of the transport equation (Ohm's law, equation 12) into the current conservation equation (equation 4) results in Laplace's equation for this quasipotential. Since the flux is known at the catalyst-layer boundary, the equivalent chemical-problem equation can be solved analytically to yield

$$\Phi = \Phi_0 + \frac{4F}{\sigma} Q_\Phi \tag{43}$$

To solve the geometric problem, the same *z*-plane to *w*-plane and inverse transformations can be used. Thus, the *w*-plane values (equation 36) remain the same. The difference is in the transformation from the *w*-plane to a different *a*-plane, denoted as the a_Φ-plane, because now the left side should be segment ED and the bottom should be EB instead of AE and AB, respectively (see Figure 4). Thus, the correct Schwartz-Christoffel transformation is

$$a_\Phi = -\int_e^w \frac{dw}{\sqrt{w+c}\sqrt{w-1}\sqrt{w-c}\sqrt{w-e}} \tag{44}$$

which again has to be evaluated numerically. The boundary condition transformation then becomes

$$\left.\frac{\partial Q_\Phi}{\partial a_{\Phi r}}\right|_{\mathbf{BC}} = -\frac{t}{2kK(k)} N\left[Q, Q_\Phi\right] \frac{\sqrt{u-e}}{\sqrt{u+1}} = G_\Phi\left[Q, Q_\Phi, a_{\Phi i}\right] \tag{45}$$

and the series solution is

$$Q_\Phi = c_{\Phi_0} a_{\Phi r} + \sum_{n=1}^{\infty} c_{\Phi n} \cos\left(\frac{\pi n}{a_{\Phi_C}} a_{\Phi i}\right) \sinh\left(\frac{\pi n}{a_{\Phi_C}} a_{\Phi r}\right) \tag{46}$$

with the coefficients given by

$$c_{\Phi_0} = \frac{\int_0^{a_{\Phi \mathbf{C}}} G_\Phi\left[Q, Q_\Phi, a_{\Phi i}\right] da_{\Phi i}}{a_{\Phi \mathbf{C}}}; \quad c_{\Phi n} = \frac{2\int_0^{a_{\Phi \mathbf{C}}} \cos\left(\frac{\pi n}{a_{\Phi \mathbf{C}}} a_{\Phi i}\right) G_\Phi\left[Q, Q_\Phi, a_{\Phi i}\right] da_{\Phi i}}{\pi n \cosh\left(\frac{\pi n}{a_{\Phi \mathbf{C}}} a_{\Phi \mathbf{B}}\right)} \tag{47}$$

Thus, one again only needs to integrate along **BC**, this time in the a_Φ-plane, to determine Q_Φ.

6. Overall solution procedure

The overall solution procedure is to solve for the two quasipotentials simultaneously by integrating on **BC** in their respective planes and using the chemical model to obtain the correct values for the variables. The equations are all given above and in this section the solution procedure is summarized. Because of the use of the two quasipotentials and the need to ensure that all of the variables are evaluated at the same points, a Gauss-Legendre integration method is used. Thus, the integration points on **BC** are specified in the a- and a_Φ-planes, thereby allowing one to switch between those planes as well as with the w-plane, since the values of u on **BC** are needed to evaluate G and G_Φ (see equations 40 and 45, respectively). Therefore, a substantial amount of bookkeeping is required. For the integration, 25 points are used and for Q and Q_Φ, a 20 term series is used.

The overall solution procedure can be summarized by the following steps.

1. Calculate the relevant dimensions and points in the *w*-plane. This involves determining *k* using equation 33, and then calculating the other points using equation 36.
2. Calculate the location of **B** and **C** in the *a*- and a_Φ-planes using the transformations given by equations 37 and 44, respectively.
3. Calculate the *a* and a_Φ points along **BC** needed for the Gauss-Legendre integration; and also determine the corresponding *u* points for each of these in the *w*-plane and the other *a*- or a_Φ-plane.
4. Guess a value of the flux boundary condition at the catalyst layer, $N[Q,Q_\Phi]$.
5. Calculate $G[Q,Q_\Phi,a_i]$ and $G_\Phi[Q,Q_\Phi,a_{\Phi_i}]$ using equations 40 and 45, respectively; and integrate to get the Fourier coefficient values in the series solutions, equations 42 and 47, respectively.
6. Calculate the values of *Q* and Q_F along **BC** using equations 41 and 46, respectively.
7. Use the chemical-problem ODEs (equations 22 thru 28) to get the values for the various variables along **BC** and calculate the boundary-condition flux using equation 29.
8. Check the calculated flux with the guessed flux and iterate until achieve convergence.

Out of the above steps, steps 1 thru 3 are only required once per given geometry (*t*, *L*, and δ). Steps 5 thru 8 represent an iteration loop. The above solution procedure is perhaps not the most robust or efficient way to solve the problem; the optimization of the solution procedure is beyond the cope of this paper. Finally, if desired, once the problem is solved, one can calculate contours in the *z*-plane using the values of *Q* and Q_Φ and the relevant transformations. As a benchmark, typical solution times for a problem are a minute or so on a desktop computer. Before

proceeding to examine simulation results, comments on the treatment of multilayer DM is necessary.

7. Application to a multilayer diffusion medium

As mentioned in the introduction, DM are often composed of multiple layers. Typically this is a macroporous substrate layer and microporous layer (MPL) next to the catalyst layer. The MPL serves to provide good contact between the DM and the catalyst layer will also playing a role in cell water and thermal management [44, 11, 27, 14, 32, 45, 13, 24, 16, 25, 39]. The MPL is typically dense, with small hydrophobic pores. To treat MPLs and multilayer DM in general, the following approach is utilized.

The difference between the MPL and macroporous GDL is only in terms of the dependent properties. The governing equations remain the same throughout all the layers of the DM. Thus, the geometric problem is identical (with different values along **BC**), and hence one only requires a methodology to determine the correct set of material-property expressions to use in the chemical-model equations. This is done by separating the chemical-model integration for each specified Gaussian integration point in the a- or a_Φ-planes,

$$\left\{p_{\mathrm{L}}, y_{\mathrm{O}_2}, T, \ldots\right\} = \int_0^Q \left\{\mathrm{ODE}(Q)\right\} \mathrm{d}Q = \int_0^{Q_{tran}} \left\{\mathrm{ODE}_{\mathrm{GDL}}(Q)\right\} \mathrm{d}Q + \int_{Q_{tran}}^Q \left\{\mathrm{ODE}_{\mathrm{MPL}}(Q)\right\} \mathrm{d}Q \tag{48}$$

where the set of values represent the chemical-model ODEs, the subscripts denote the regions, and Q_{tran} is the transition point from the GDL to the MPL. This transition point can be determine by mapping the MPL / GDL boundary in the z-plane to the other planes, as shown in Figure 7 for the a-plane. To implement this method, one calculates the Q_{tran} points for the **BC** Gaussian integration points in step 3 of the solution method outline above. Then, when solving the initial-

value ODEs, one utilizes equation 48. This treatment will create a slope change in the curves in Figure 3 when Q_{tran} is reached. Obviously, this method is assuming more or less line integrations and changes in the MPL occur primarily in the *x* direction. Since the MPLs are relatively thin, this should not be a major source of error. While the above method is not rigorous, it does allow the use of the quasipotential transformation for multilayer DMs with minimal error; to be fully rigorous, the quasipotential would have to become spatially dependent and one losses its attractiveness for use.

8. Results and discussion

The above described model can provide many insights depending on what is being focused upon. In this section, we focus on a couple of issues, namely, the cause of flooding and the relationship between thermal and water management, the effect of the rib/channel geometry on performance and oxygen concentration, and the impact of having an MPL. For the analyses presented in this section, the inlet values and input parameters are given in Table II, and the material properties are presented above in Table I. The input parameters are typical values as determined by our earlier simulations with all of the cell layers but where we did not account for the rib/channel effect [38]. A potential of 0.6 V is chosen since this corresponds to the expected cell potential in an automotive fuel cell. The use of the values in Table II, especially concerning the assumption of uniform values in the catalyst layer, limits the accuracy of the simulation results, however, some general trends can be examined and insight gained.

One can use the chemical model to do a relatively simple analysis of the effect of DM wettability or hydrophilicity. Since the chemical model is being used, a value of *Q* is chosen that corresponds to a current density of 1 A/cm^2 and a DM thickness of 250 μm (*i.e.*, $Q = 1.3 \times 10^{-7}$

mol / cm s). As discussed with Figure 3, the value of Q where the oxygen partial pressure goes towards zero can be seen as a limiting current density. Furthermore, it is suspected that the decrease in gas-phase pressure can result in flooding and perhaps has a greater effect than the increase in the liquid pressure. To examine some of these issues and also the impact of the heat-pipe effect, simulation results are shown in Figure 6.

From the figure, one can see that as the hydrophilicity is increased from a pure hydrophobic to a mainly hydrophilic DM, the oxygen partial pressure decreases, nominally due to increased blockage of the pores by liquid water, *i.e.*, flooding. Furthermore, for the assumed DM thickness, the figure shows that 1 A/cm^2 is the limiting current density when the hydrophilic pore fraction is 80 % or less depending on the absolute permeability of the DM. The effect of absolute permeability is relatively straightforward, since as the permeability decreases, the resistance to gas and liquid flow increases, thereby causing more significant water flooding throughout the DM.

Flooding is a combined result of the intrinsic decrease in the gas-phase volume fraction due to having a more hydrophilic medium and an increase in the capillary pressure, which is defined as the liquid minus the gas pressure. In terms of capillary pressure, intuition states that as the DM becomes more hydrophobic, the increase in the liquid pressure will cause more flooding than the gas-pressure decrease. Conversely, as the DM becomes hydrophilic, the decrease in the gas pressure will cause more flooding than the liquid-pressure increase. The interplay between these effects is seen in Figure 6, where the oxygen partial pressure exhibits a maximum with respect to the fraction of hydrophilic pores. This maximum becomes sharper as the permeability decreases since flow resistance becomes more dominant in the system and the capillary-pressure effect on flooding begins to outweigh the intrinsic hydrophilicity effect. In agreement with

Figure 3, it seems that the decrease in the gas pressure results in more significant flooding than the increase in the liquid pressure based on the shape of the curves in Figure 6 at the high and low hydrophilicity levels, respectively. Finally, it seems that a hydrophilic pore fraction around 20 % results in optimal water-balance performance.

Figure 6 also compares nonisothermal and isothermal simulations. This comparison allows one to quantify the heat-pipe effect on PEFC performance and the DM. The heat-pipe effect occurs with saturated gas feeds where water will evaporate at the catalyst layer and condense at the gas channel due to the temperature gradient within the DM. This effect impacts performance both beneficially and detrimentally [38]. On the beneficial side, it removes liquid water by transferring it into the vapor phase, thereby decreasing flooding. On the detrimental side, the incoming oxygen gases must now diffuse against a counterflow of water vapor that is moving along the temperature gradient instead of with the incoming oxygen. The interplay between these two effects is clearly seen in Figure 6. For the cases where flooding is important (*e.g.*, at low permeabilities or high hydrophilic pore fractions), the heat-pipe effect is overall beneficial and the nonisothermal case results in higher oxygen partial pressure than the isothermal one. However, there is a switching point where the detrimental effects of the heat pipe outweigh the beneficial ones for conditions where flooding is less important. This results in a crossover of the curves under these conditions such that the isothermal case results in higher partial pressures than the nonisothermal one. In all, Figure 6 demonstrates that water and thermal management are intricately linked and that mathematical modeling provides a route to begin to optimize the operating conditions and material properties.

The full model can be used to assess the impact of the rib and channel on performance. To visualize the transformation and to see the resulting profiles, Q is given in both the a- and z-

planes in Figure 7. As shown in Figure 3, as Q increases, the temperature and liquid pressure increase and the partial pressure of oxygen decreases. Therefore, Figure 7 clearly shows in the real or z-plane a buildup of liquid water under the rib and a subsequent lower amount of oxygen available for reaction. The Q profile also shows that there are not significant gradients under the rib, except perhaps near the channel and also somewhat near the catalyst layer. The latter is driven by the reaction rate distribution as discussed later. If one envisions an entire flow channel, the *Q* profile demonstrates that the maximum concentration of oxygen starts at the middle of the channel (*i.e.*, the symmetry line at $y = 0$) as expected, but then forms two maxima and a resulting minima in the channel middle. This shape is due to the effect of the interplay of gas diffusion and the reaction-rate distribution.

It is of interest to examine the effect of the rib / channel ratio. To do this, the maximum, minimum, and average current densities are tabulated as a function of the relative size of the channel and rib and are given in Figure 8a. From these values, an optimum value of around 65 % channel is obtained. However, such a study ignores the impact of manufacturability of the flowfield, type of flow path (*e.g.*, serpentine versus straight channels), and mechanical effects of the rib. The optimum in current density arises from the fact that at large channels (small ribs), transport of the electronic current is limiting and at small channels (large ribs) transport of the oxygen becomes limiting. The oxygen overall is more limiting, which is why the optimum is shifted towards larger channels than ribs and the decrease is longer and more severe with smaller channels than with smaller ribs. The current-density spread for a given channel to rib ratio has a complex shape, with the smallest spread (*i.e.*, the most uniform current-density distribution) occurring at the optimum channel to rib ratio. The spread then becomes larger as the current-

density distribution becomes more nonuniform, with again, a larger spread observed with smaller channels than with smaller ribs due to the dominant oxygen-transport limitations.

While Figure 8a shows the range of current density, it does not indicate the current-density distribution. Figure 8b shows distributions for three channel-to-rib ratios. It is clear that the three cases have vastly different current-density distributions. Furthermore the locations of the maximum and minimum values reported in Figure 8a can occur at different points along the curve. Essentially, the maximum value is the point at which the various transport limitations are minimal and occurs near the rib/channel interface because there is not significant redistribution of current and oxygen in the DM, and helps to explain the profiles in Figure 7. It does shift to more under the rib with larger channels, since this does allow more oxygen redistribution. The minimum current density occurs near the top of the rib because of oxygen limitations. However, as the ribs become smaller, the dominant limiting phenomena changes and the minimum shifts towards the bottom of the channel. Overall, the impact of the rib and channel can generate very nonuniform current-density distributions, especially as one moves far away from the optimum value for the set of operating conditions and material properties.

Finally, the impact of a multilayer DM can be investigated. This analysis is shown in Figure 9 for the oxygen partial pressure. For these simulations, the same current density is examined in order to see better the MPL effect since it will result in the same oxygen flux. However, because the case with the MPL demonstrates worse performance, this required that the cell voltage be lowered about 20 mV compared to the non-MPL case. The reason for this decrease is due to the resulting thicker layer (270 vs. 250 μm) and the buildup of liquid water next to the catalyst layer and a greater temperature gradient caused by the more resistive MPL. The decrease in the liquid water under the rib is primarily due to the increased temperature. However, near the catalyst

layer, this gain is offset by the increased buildup of liquid water, as shown in Figure 9. Typically, MPLs result in better performance, which is not captured by the simulation because the buildup of liquid water will cause more water to move towards the anode [39]. However, this link is missing in the current simulation where the net water flux through the membrane, β_w, is set and does not vary. Finally, Figure 9b shows the current-density distribution for the two cases. Clearly, the impact of the MPL is significant and causes a shift in the maximum current density towards the channel and away from the rib/channel interface. This demonstrates that the flooding and oxygen limitation caused by the MPL are more significant than its effect on the electronic conductivity.

9. Summary

In this paper, a quasipotential approach along with conformal mapping has been used to model the diffusion media (DM) of a polymer-electrolyte fuel cell. This method goes beyond previous approaches and removes previous limitations of isothermal operation, placement of the electronic-potential boundary condition, neglect of two-phase flow, and examination of only single-layer diffusion media. The presented method provides a series solution that is grid independent and only requires integration along a single boundary. As applied to the cathode DM, simulations showed the complex interplay between water and thermal management and performance, the importance of gas-phase pressure decreases, the impact of the rib-to-channel ratio on the current-density distribution and performance, the existence of diffusion under the rib and water buildup, and the impact of having a multilayer DM with a microporous layer.

This last analysis highlighted some of the current limitations of the method. Primarily, there are three principal values that must be assumed at the catalyst layer interface and were taken to

be constant. Ideally, these values should be determined using models of the porous electrode, membrane, and anode side of the cell. This can be implemented using 1-D models for those layers at each Gaussian integration point, and this approach is currently under investigation. Also under investigation is using the model in a 1+2-D arrangement where the composition along the gas channel varies and the presented model can be run in the various segments. However, as these conditions change, so to would the values of the assumed catalyst-layer values, again necessitating some kind of model for the catalyst layer and rest of the cell. Another limitation of the method is the perhaps the improper placement of the temperature boundary condition, and this needs to be quantified. Another effect to be quantified is that the material properties of the medium have to be assumed isotropic for the quasipotential transformation, which is not necessarily in agreement with experimental data. A possible extension of the model would be to include a first-order, macroscopic mechanical force balance, which will enable one to examine how compression on the DM by the ribs changes the overall performance. Finally, other improvements for the model include optimizing the mathematics and the numerical solution along the boundary to be more robust and less computationally costly.

Acknowledgements

This work was supported by the Assistant Secretary for Energy Efficiency and Renewable Energy, Office of Hydrogen, Fuel Cell, and Infrastructure Technologies, of the U. S. Department of Energy under contract number DE-AC02-05CH11231 and by industrial partners.

References

[1] *CRC Handbook of Chemistry and Physics*, CRC Press, Boca Raton, FL, 1979.

[2] N. I. Akhiezer, *Elements of the Theory of Elliptic Functions*, American Mathematical Society, Providence, RI, 1990.

[3] D. R. Baker, *Reducing Nonlinear-Systems of Transport-Equations to Laplaces-Equation*, Siam Journal on Applied Mathematics, 53 (1993), pp. 419-439.

[4] D. R. Baker, M. W. Verbrugge and J. Newman, *A Transformation for the Treatment of Diffusion and Migration - Application to Stationary Disk and Hemisphere Electrodes*, Journal of Electroanalytical Chemistry, 314 (1991), pp. 23-44.

[5] R. B. Bird, W. E. Stewart and E. N. Lightfoot, *Transport Phenomena*, John Wiley & Sons, Inc., New York, 2002.

[6] R. Bradean, K. Promislow and B. Wetton, *Transport Phenomena in the Porous Cathode of a Proton Exchange Membrane Fuel Cell*, Numerical Heat Transfer Part a-Applications, 42 (2002), pp. 121-138.

[7] C. H. Chao and A. J. J. Hwang, *Predictions of Phase Temperatures in a Porous Cathode of Polymer Electrolyte Fuel Cells Using a Two-Equation Model*, Journal of Power Sources, 160 (2006), pp. 1122-1130.

[8] F. A. L. Dullien, *Porous Media: Fluid Transport and Pore Structure*, Academic Press, Inc., New York, 1992.

[9] J. P. Feser, A. K. Prasad and S. G. Advani, *Experimental Characterization of in-Plane Permeability of Gas Diffusion Layers*, Journal of Power Sources, 162 (2006), pp. 1226-1231.

[10] V. Gurau, M. J. Bluemle, E. S. De Castro, Y. M. Tsou, T. A. Zawodzinski and J. A. Mann, *Characterization of Transport Properties in Gas Diffusion Layers for Proton Exchange Membrane Fuel Cells 2. Absolute Permeability*, Journal of Power Sources, 165 (2007), pp. 793-802.

[11] N. Hara, K. Tsurumi and M. Watanabe, *An Advanced Gas Diffusion Electrode for High Performance Phosphoric Acid Fuel Cells*, Journal of Electroanalytical Chemistry, 413 (1996), pp. 81-88.

[12] F. B. Hildebrand, *Advanced Calculus for Applications, 2nd Ed.*, Prentice-Hall, Englewood Cliffs, NJ, 1976.

[13] G. J. M. Janssen and M. L. J. Overvelde, *Water Transport in the Proton-Exchange-Membrane Fuel Cell: Measurements of the Effective Drag Coefficient*, Journal of Power Sources, 101 (2001), pp. 117-125.

[14] K. Karan, H. Atiyeh, A. Phoenix, E. Halliop, J. Pharoah and B. Peppley, *An Experimental Investigation of Water Transport in PEMFCs - the Role of Microporous Layers*, Electrochemical and Solid State Letters, 10 (2007), pp. B34-B38.

[15] A. Kazim, H. T. Liu and P. Forges, *Modelling of Performance of PEM Fuel Cells with Conventional and Interdigitated Flow Fields*, Journal of Applied Electrochemistry, 29 (1999), pp. 1409-1416.

[16] C. S. Kong, D.-Y. Kim, H.-K. Lee, Y.-G. Shul and T.-H. Lee, *Influence of Pore-Size Distribution of Diffusion Layer on Mass-Transport Problems of Proton Exchange Membrane Fuel Cells*, Journal of Power Sources, 108 (2002), pp. 185-191.

[17] A. A. Kulikovsky, J. Divisek and A. A. Kornyshev, *Modeling the Cathode Compartment of Polymer Electrolyte Fuel Cells: Dead and Active Reaction Zones*, Journal of the Electrochemical Society, 146 (1999), pp. 3981-3991.

[18] E. C. Kumbur, K. V. Sharp and M. M. Mench, *On the Effectiveness of Leverett Approach for Describing the Water Transport in Fuel Cell Diffusion Media*, Journal of Power Sources, 168 (2007), pp. 356-368.

[19] G. Y. Lin, W. S. He and T. Van Nguyen, *Modeling Liquid Water Effects in the Gas Diffusion and Catalyst Layers of the Cathode of a PEM Fuel Cell*, Journal of the Electrochemical Society, 151 (2004), pp. A1999-A2006.

[20] J. P. Meyers, R. D. Villwock, R. M. Darling and J. Newman, *Multicomponent Diffusion in a Gas-Diffusion Electrode with a Ribbed Flow Field Using a Quasipotential Transformation*, in J. W. Van Zee, T. F. Fuller, P. C. Foller and F. Hine, eds., *Advances in Mathematical Modeling and Simulation of Electrochemical Processes and Oxygen Depolarized Cathodes and Activated Cathodes for Chlor-Alkali Processes*, The Electrcohemical Society Proceedings Series, Pennington, NJ, 1998.

[21] J. H. Nam and M. Kaviany, *Effective Diffusivity and Water-Saturation Distribution in Single- and Two-Layer PEMFC Diffusion Medium*, International Journal of Heat and Mass Transfer, 46 (2003), pp. 4595-4611.

[22] D. Natarajan and T. V. Nguyen, *A Two-Dimensional, Two-Phase, Multicomponent, Transient Model for the Cathode of a Proton Exchange Membrane Fuel Cell Using Conventional Gas Distributors*, Journal of the Electrochemical Society, 148 (2001), pp. A1324-A1335.

[23] K. C. Neyerlin, W. B. Gu, J. Jorne and H. A. Gasteiger, *Determination of Catalyst Unique Parameters for the Oxygen Reduction Reaction in a PEMFC*, Journal of the Electrochemical Society, 153 (2006), pp. A1955-A1963.

[24] V. A. Paganin, E. A. Ticianelli and E. R. Gonzalez, *Development and Electrochemical Studies of Gas Diffusion Electrodes for Polymer Electrolyte Fuel Cells*, Journal of Applied Electrochemistry, 26 (1996), pp. 297-304.

[25] U. Pasaogullari and C. Y. Wang, *Two-Phase Transport and the Role of Micro-Porous Layer in Polymer Electrolyte Fuel Cells*, Electrochimica Acta, 49 (2004), pp. 4359-4369.

[26] U. Pasaogullari, C. Y. Wang and K. S. Chen, *Two-Phase Transport in Polymer Electrolyte Fuel Cells with Bilayer Cathode Gas Diffusion Media*, Journal of the Electrochemical Society, 152 (2005), pp. A1574-A1582.

[27] E. Passalacqua, G. Squadrito, F. Lufrano, A. Patti and L. Giorgi, *Effects of the Diffusion Layer Characteristics on the Performance of Polymer Electrolyte Fuel Cell Cathodes*, Journal of Applied Electrochemistry, 31 (2001), pp. 449-454.

[28] R. H. Perry and D. W. Green, *Perry's Chemical Engineers' Handbook*, McGraw-Hill, New York, 1997.

[29] B. Pillay and J. Newman, *Modeling Diffusion and Migration in Dilute Electrochemical Systems Using the Quasi-Potential Transformation*, Journal of the Electrochemical Society, 140 (1993), pp. 414-420.

[30] W. H. Press, S. A. Teukolsky, W. T. Vetterling and B. P. Flannery, *Numerical Recipes in Fortran 77, 2nd Ed.*, Cambridge University Press, Cambridge, 1992.

[31] K. Promislow, J. Stockie and B. Wetton, *A Sharp Interface Reduction for Multiphase Transport in a Porous Feul Cell Electrode*, Proceedings of the Royal Society of London, Series A: Mathematical and Physical Sciences, 462 (2006), pp. 789.

[32] Z. G. Qi and A. Kaufman, *Improvement of Water Management by a Microporous Sublayer for PEM Fuel Cells*, Journal of Power Sources, 109 (2002), pp. 38-46.

[33] A. A. Shah, G. S. Kim, W. Gervais, A. Young, K. Promislow, J. Li and S. Ye, *The Effects of Water and Microstructure on the Performance of Polymer Electrolyte Fuel Cells*, Journal of Power Sources, 160 (2006), pp. 1251-1268.

[34] M. W. Verbrugge, D. R. Baker and J. Newman, *Dependent-Variable Transformation for the Treatment of Diffusion, Migration, and Homogeneous Reactions - Application to a Corroding Pit*, Journal of the Electrochemical Society, 140 (1993), pp. 2530-2537.

[35] Z. H. Wang, C. Y. Wang and K. S. Chen, *Two-Phase Flow and Transport in the Air Cathode of Proton Exchange Membrane Fuel Cells*, Journal of Power Sources, 94 (2001), pp. 40-50.

[36] A. Z. Weber, R. Balliet, H. P. Gunterman and J. Newman, *Modeling Water Management in Polymer-Electrolyte Fuel Cells*, in M. Schlesinger, ed., *Modern Aspects of Electrochemistry, Vol. 43*, Springer, New York, 2008.

[37] A. Z. Weber, R. M. Darling and J. Newman, *Modeling Two-Phase Behavior in PEFCs*, Journal of the Electrochemical Society, 151 (2004), pp. A1715-A1727.

[38] A. Z. Weber and J. Newman, *Coupled Thermal and Water Management in Polymer-Electrolyte Fuel Cells*, Journal of the Electrochemical Society, 153 (2006), pp. A2205-A2214.

[39] A. Z. Weber and J. Newman, *Effects of Microporous Layers in Polymer Electrolyte Fuel Cells*, Journal of the Electrochemical Society, 152 (2005), pp. A677-A688.

[40] A. Z. Weber and J. Newman, *Modeling Gas-Phase Flow in Porous Media*, International Communications in Heat and Mass Transfer, 32 (2005), pp. 855-860.

[41] A. Z. Weber and J. Newman, *Modeling Transport in Polymer-Electrolyte Fuel Cells*, Chemical Reviews, 104 (2004), pp. 4679-4726.

[42] A. Z. Weber and J. Newman, *Transport in Polymer-Electrolyte Membranes. II. Mathematical Model*, Journal of the Electrochemical Society, 151 (2004), pp. A311-A325.

[43] A. C. West and T. F. Fuller, *Influence of Rib Spacing in Proton-Exchange Membrane Electrode Assemblies*, Journal of Applied Electrochemistry, 26 (1996), pp. 557-565.

[44] M. S. Wilson, J. A. Valerio and S. Gottesfeld, *Low Platinum Loading Electrodes for Polymer Electrolyte Fuel Cells Fabricated Using Thermoplastic Ionomers*, Electrochimica Acta, 40 (1995), pp. 355-363.

[45] Z. G. Zhan, J. S. Xiao, D. Y. Li, M. Pan and R. Z. Yuan, *Effects of Porosity Distribution Variation on the Liquid Water Flux through Gas Diffusion Layers of PEM Fuel Cells*, Journal of Power Sources, 160 (2006), pp. 1041-1048.

[46] D. Zwillinger, ed., *Crc Mathematical Tables and Formulae, 31st Ed.*, CRC Press, Inc., Boca Raton, FL, 2003.

Captions

Table I. Relevant material and transport properties, the other fluid properties and diffusion coefficients can readily be obtained through handbooks [1, 28].

Table II. Required simulation inlet conditions and catalyst-layer parameters.

Figure 1. Polymer-electrolyte-fuel-cell schematic showing the reactant-gas and charged-species transport. The cell consists of gas flowfields, diffusion media, catalyst layers, and a proton-conducting ionomer. The highlighted box is the region treated in this paper.

Figure 2. Schematic of the modeling domain showing the boundary conditions, variables solved for, and the governing equations. The numbers in the brackets correspond to the equations in the text.

Figure 3. Results of the chemical model for the gas and liquid pressure, the temperature, and the gas-phase mole fractions as a function of the quasipotential. The material properties are given in Table I.

Figure 4. Schematic of the solution of the geometric problem using conformal mapping including the boundary conditions and known boundary points in the z-plane.

Figure 5. Transformation of the MPL / GDL interface from the z-plane to the a-plane.

Figure 6. Oxygen partial pressure at the catalyst layer as a function of DM hydrophilicity for different DM absolute permeabilities and isothermal (gray) and nonisothermal (black) simulations. The chemical model is used assuming a 1 A/cm^2 current

density with the Table II inlet conditions and the Table I GDL properties for those that are not varied.

Figure 7. Contour plot of Q in the a- and z-planes for the parameters from Table I and Table II and with a dimensionless channel length of $\delta = 0.5$.

Figure 8. (a) Maximum, minimum, and average current density as a function of dimensionless channel size using the parameters from Table I and Table II. (b) Current-density distribution for three dimensionless channel sizes.

Figure 9. (a) Contour plot of the partial pressure of oxygen both with (right) and without (left) a MPL, which is marked in the figure. (b) Current-density distribution at the catalyst layer for the two cases. The parameters from Table I and Table II and with a dimensionless channel length of $\delta = 0.5$.

Table I. Relevant material and transport properties, the other fluid properties and diffusion coefficients can readily be obtained through handbooks [1, 28].

Independent Property		**Value**		
Specific interfacial area	at_{CL}	300		
ORR standard potential	U^{θ}	$1.229-9\times10^{-4}(T-298.15)$		V
ORR enthalpy potential	U_H	$1.48-1.5\times10^{-4}(T-298.15)$		V
ORR exchange current density	i_0	$5.71\times10^{-10}\exp\left[\frac{67000}{R}\left(\frac{1}{T_{\mathrm{ref}}}-\frac{1}{T}\right)\right]$		A/cm^2
		Region		
		MPL	DM	
Absolute permeability	k_{sat}	1×10^{-12}	1×10^{-9}	cm^2
Thickness	δ	20	250	μm
Thermal conductivity	k^{eff}	0.003	0.015	W/cm·K
Bulk porosity	ε_{o}	0.3	0.7	
Electrical conductivity	σ	3	7	S/cm
Pore-size distribution properties				
Characteristic radii	$r_{\mathrm{o},1}$	2	6	μm
	$r_{\mathrm{o},2}$	0.05	0.7	μm
Characteristic spreads	s_1	0.75	0.6	
	s_2	1	0.6	
Fraction that is distribution 1	$f_{r,1}$	0.5	0.95	
Fraction of hydrophilic pores	f_{HI}	0	0.3	
Hydrophobic contact angle	θ_{HO}	110	110	°
Hydrophilic contact angle	θ_{HI}	n/a	80	°

Table II. Required simulation inlet conditions and catalyst-layer parameters.

Property	Value	
Electronic potential	0.6	V
Gas and liquid pressures	1	bar
Channel relative humidity	100	%
Nitrogen mole fraction	0.62	
Temperature	339.2	K
Ionic potential, Φ_2	–0.173	V
Dimensionless net water flux, β_w	0.165	
Dimensionless net heat flux, β_q	0.21	

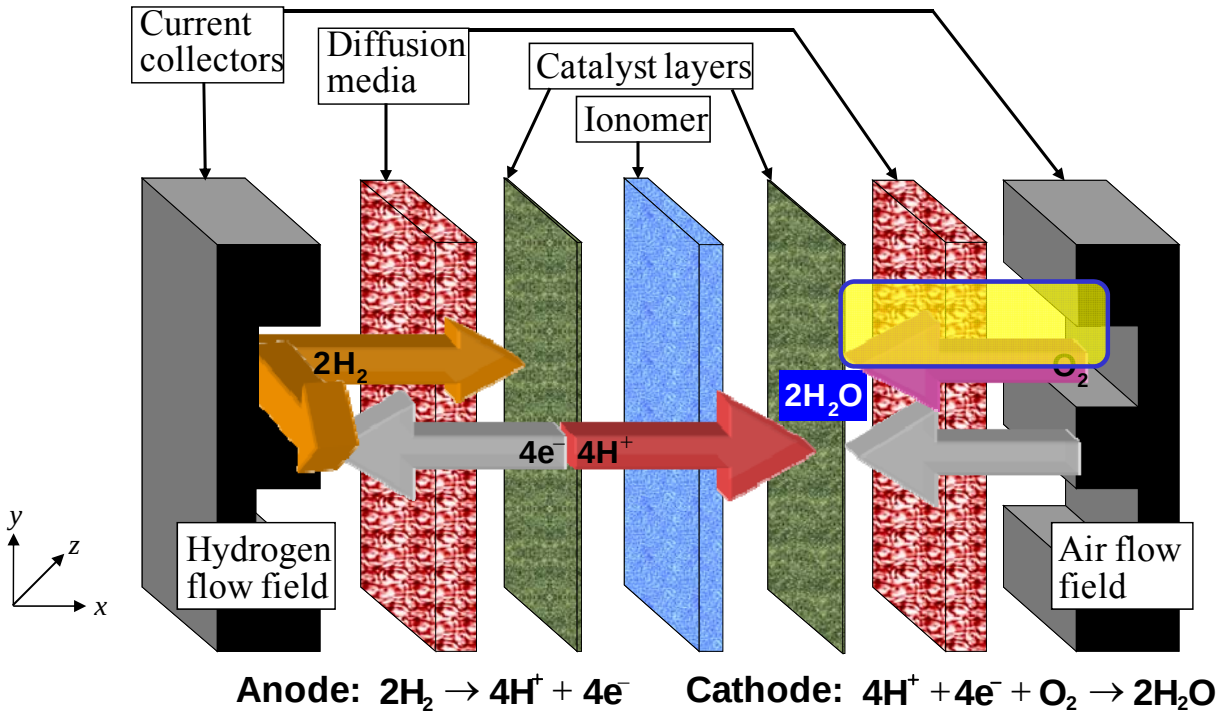

Figure 1. Polymer-electrolyte-fuel-cell schematic showing the reactant-gas and charged-species transport. The cell consists of gas flowfields, diffusion media, catalyst layers, and a proton-conducting ionomer. The highlighted box is the region treated in this paper.

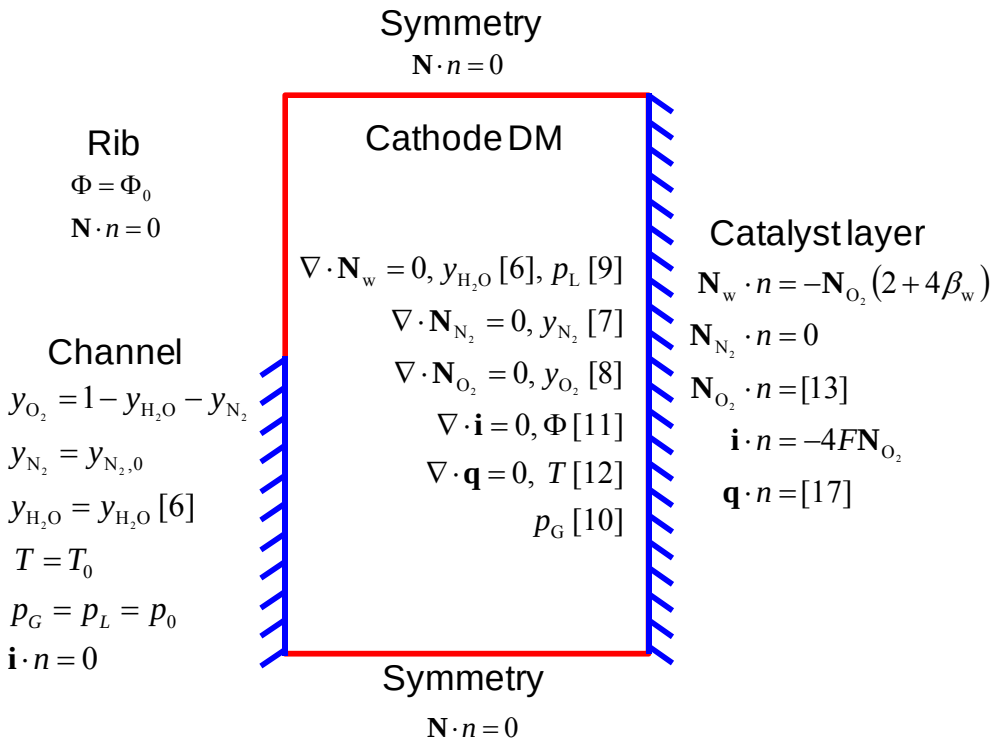

Figure 2. Schematic of the modeling domain showing the boundary conditions, variables solved for, and the governing equations. The numbers in the brackets correspond to the equations in the text.

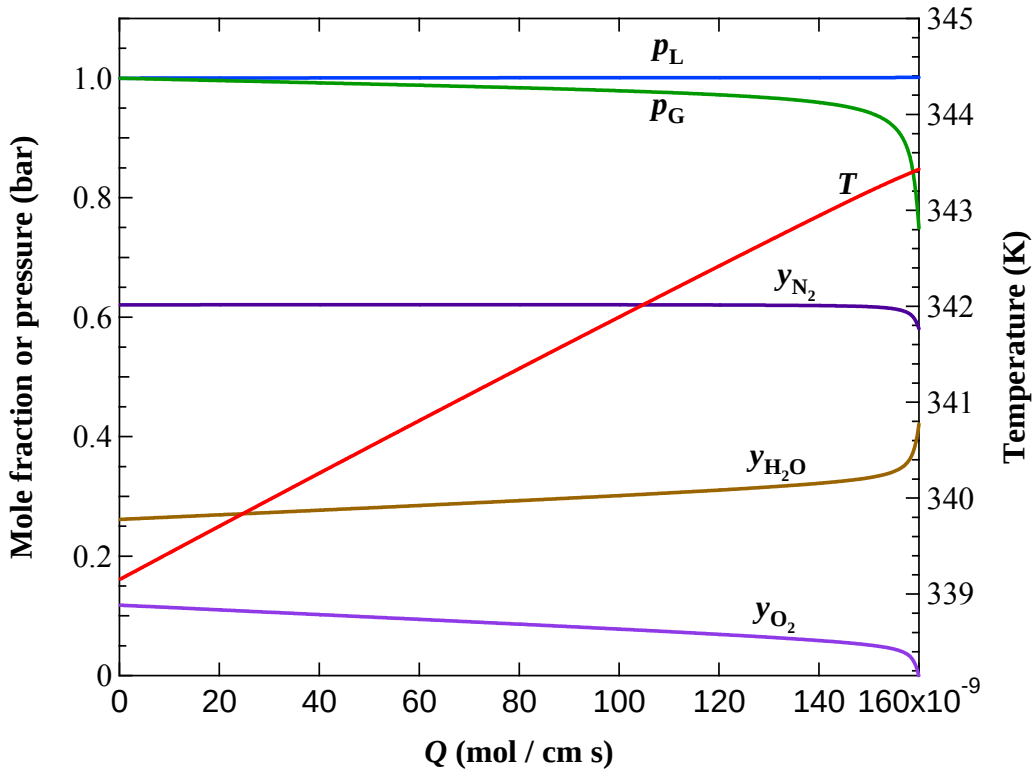

Figure 3. Results of the chemical model for the gas and liquid pressure, the temperature, and the gas-phase mole fractions as a function of the quasipotential. The material properties are given in Table I.

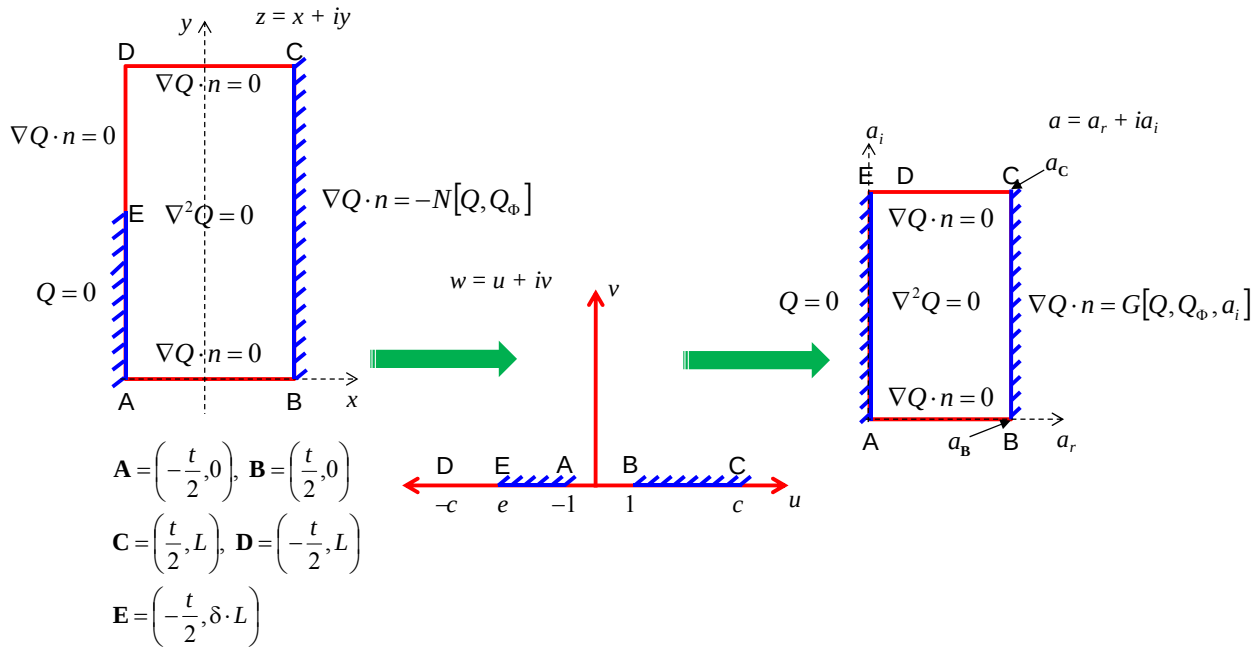

Figure 4. Schematic of the solution of the geometric problem using conformal mapping including the boundary conditions and known boundary points in the z-plane.

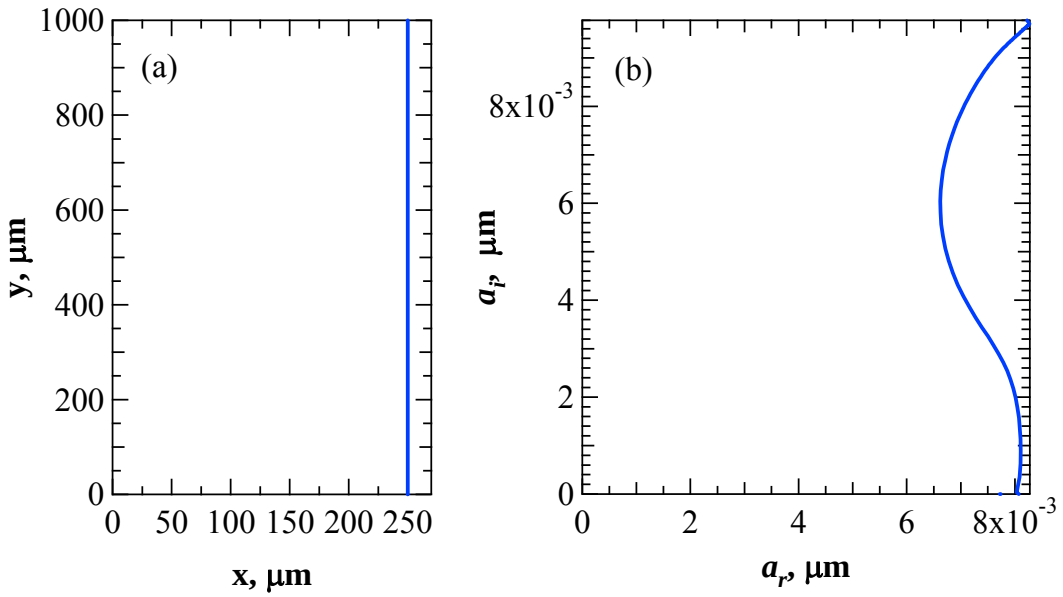

Figure 5. Transformation of the MPL / GDL interface from the *z*-plane to the *a*-plane.

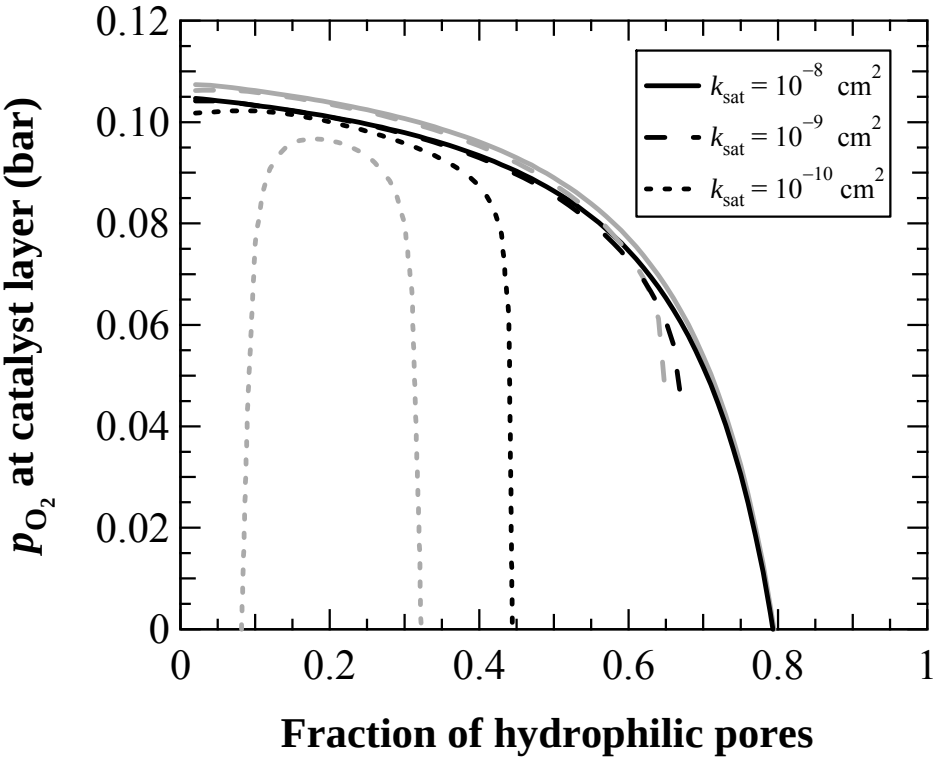

Figure 6. Oxygen partial pressure at the catalyst layer as a function of DM hydrophilicity for different DM absolute permeabilities and isothermal (gray) and nonisothermal (black) simulations. The chemical model is used assuming a 1 A/cm2 current density *with* the Table II inlet conditions and the Table I GDL properties for those that are not varied.

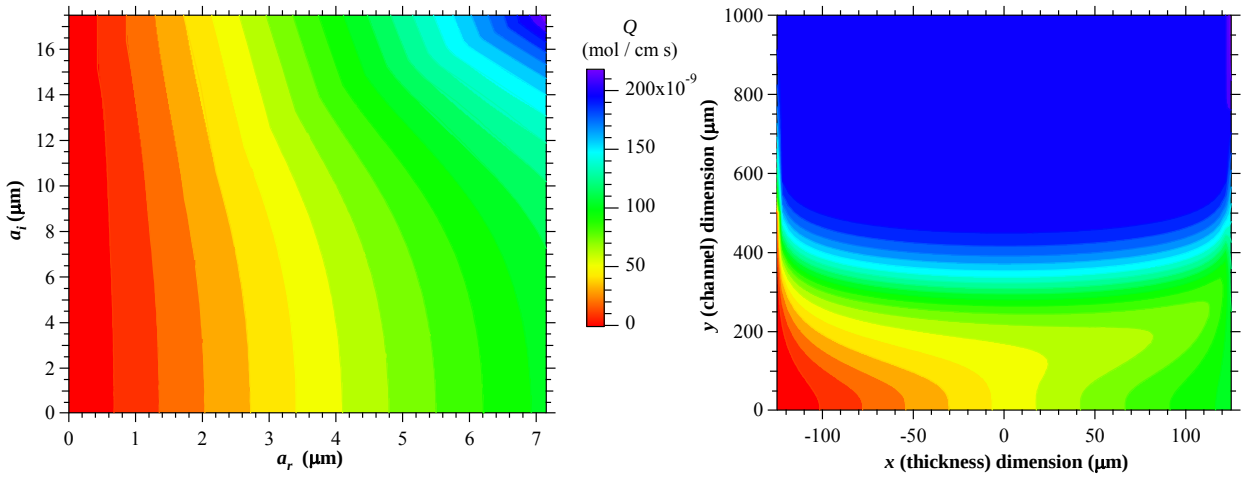

Figure 7. Contour plot of Q in the a- and z-planes for the parameters from Table I and Table II and with a dimensionless channel length of $\delta = 0.5$.

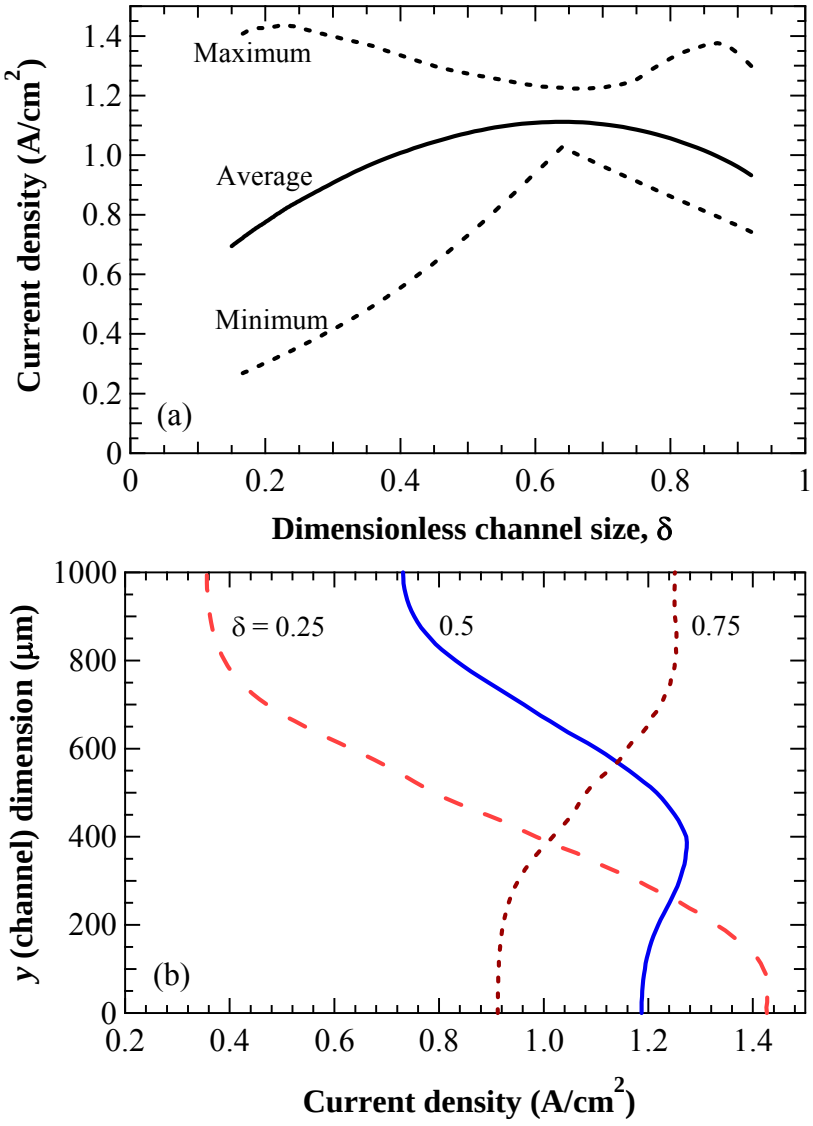

Figure 8. (a) Maximum, minimum, and average current density as a function of dimensionless channel size using the parameters from Table I and Table II. (b) Current-density distribution for three dimensionless channel sizes.

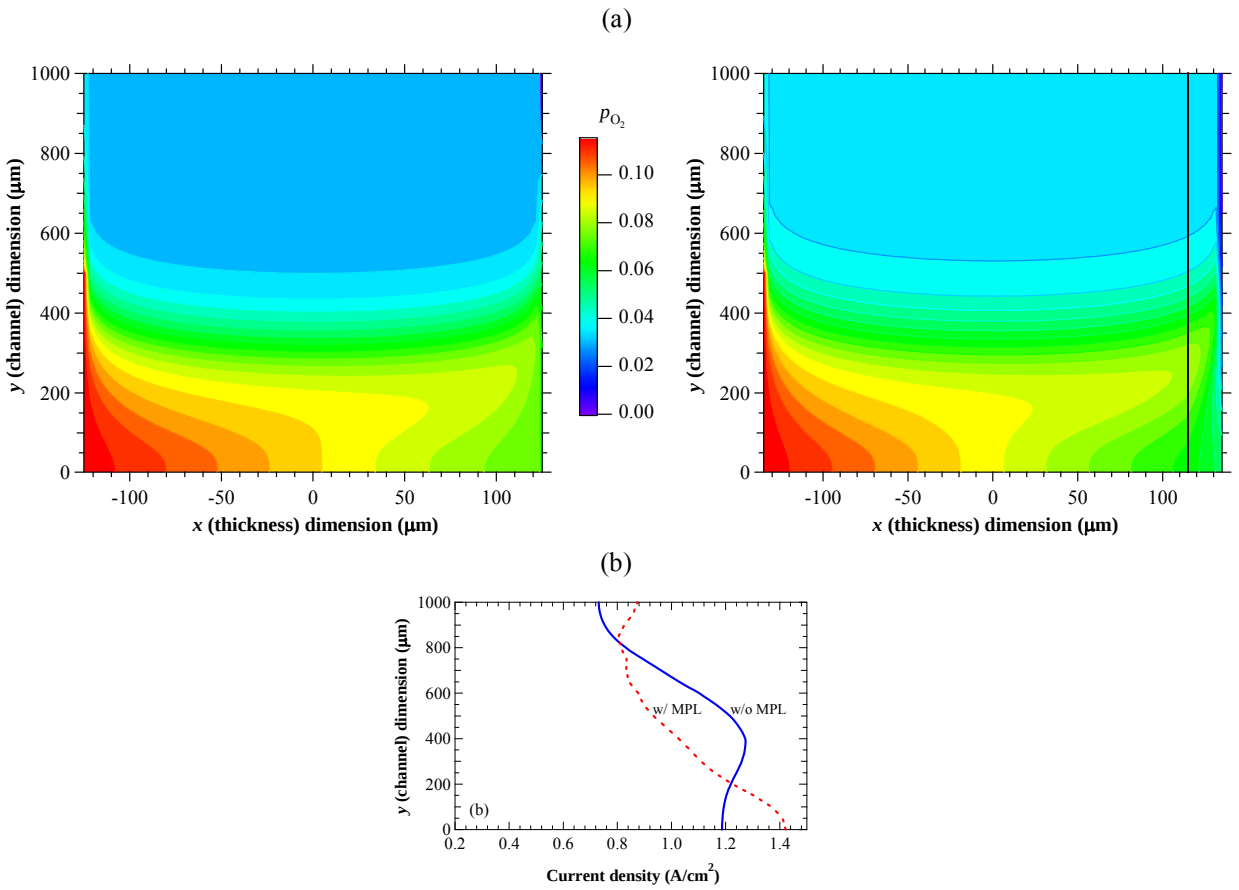

Figure 9. (a) Contour plot of the partial pressure of oxygen both with (right) and without (left) a MPL, which is marked in the figure. (b) Current-density distribution *at* the catalyst layer for the two cases. The parameters from Table I and Table II and with a dimensionless channel length of $\delta = 0.5$